Helmholtz-Zentrum Dresden-Rossendorf (HZDR)

HELMHOLTZ ZENTRUM
DRESDEN ROSSENDORF

Transitions in a magnetized quasi-laminar spherical Couette flow

Kasprzyk, C.; Kaplan, E.; Seilmayer, M.; Stefani, F.;

Originally published:

July 2017

Magnetohydrodynamics 53(2017)2, 393-401

Perma-Link to Publication Repository of HZDR:

https://www.hzdr.de/publications/Publ-25830

Release of the secondary publication
on the basis of the German Copyright Law § 38 Section 4.

TRANSITIONS IN A MAGNETIZED QUASI-LAMINAR SPHERICAL COUETTE FLOW

C. Kasprzyk[1], *E. Kaplan*[2], *M. Seilmayer*[1], *F. Stefani*[1]

[1] *Helmholtz-Zentrum Dresden–Rossendorf,*
Bautzner Landstraße 400, 01328 Dresden, Germany
[2] *Université Grenoble Alpes, CNRS, ISTerre,*
CS 40700, F-38000 Grenoble Cedex 9, France

First results of a new spherical Couette experiment are presented. The liquid metal flow in a spherical shell is exposed to a homogeneous axial magnetic field. For a Reynolds number $\mathrm{Re} = 1000$, we study the effect of increasing Hartmann number Ha. The resulting flow structures are inspected by ultrasound Doppler velocimetry. With a weak applied magnetic field, we observe an equatorially antisymmetric jet instability with the azimuthal wave number $m = 3$. As the magnetic field strength increases, this instability vanishes. When the field is increased further, an equatorially symmetric return flow instability arises. Our observations are shown to be in good agreement with linear stability analysis and non-linear flow simulations.

Introduction. The term spherical Couette flow refers to the fluid motion between two rotating spherical shells. If the liquid is electrically conducting and exposed to an external magnetic field, the set-up is sometimes called magnetized spherical Couette (MSC) flow. For the special case of resting outer cylinder, the system is completely defined by three dimensionless parameters [1]: the Reynolds number $\mathrm{Re} = \Omega_\mathrm{i} r_\mathrm{i}^2/\nu$ as a measure of the rotation (with angular velocity Ω_i of the inner sphere with radius r_i), the Hartmann number $\mathrm{Ha} = B_0 r_\mathrm{i}\sqrt{\sigma/\rho\nu}$ with B_0 denoting the strength of the applied axial magnetic field, and the geometric aspect ratio $\eta = r_\mathrm{i}/r_\mathrm{o}$ with the outer sphere radius r_o. Here, ν denotes the kinematic viscosity, ρ the density, and σ the conductivity of the fluid.

A long, albeit contentiously, discussed result of MSC flow was the observation of an angular momentum transporting magnetically induced instability in a turbulent liquid sodium flow at $\mathrm{Re} \approx 10^7$, which was described in [2] as the long sought-after magnetorotational instability (MRI). In contrast to the MRI as usually described [3], this instability was non-axisymmetric and demonstrated an equatorial symmetry whose parity depended on the strength of the applied magnetic field. Subsequent numerical investigations [4, 5] turned up a collection of induction-free instabilities related to the hydrodynamic jet instability, the Kelvin–Helmholtz-like Shercliff layer instability, and a return flow instability that replicated the parity properties, as well as the torque on the outer sphere (the proxy measurement of angular momentum transport), as documented in [2].

In order to study these types of instability in more detail, the new apparatus HEDGEHOG (Hydromagnetic Experiment with Differentially Gyrating sphEres HOlding GaInSn) has been installed at Helmholtz-Zentrum Dresden–Rossendorf (HZDR). In contrast to [2], HEDGEHOG operates in a quasi-laminar regime with two possible aspect ratios $\eta = 0.35,\ 0.5$. Numerical reference data is available for both cases [4, 6]. Its typical operating parameters, $\mathrm{Re} \sim 10^{3\ldots4}$ and $\mathrm{Ha} \sim 10^{2\ldots3}$, place HEDGEHOG in a wider class of experiments dealing with inductionless instabilities, such as the helical [7] and azimuthal MRIs [8], and the Tayler instability [9].

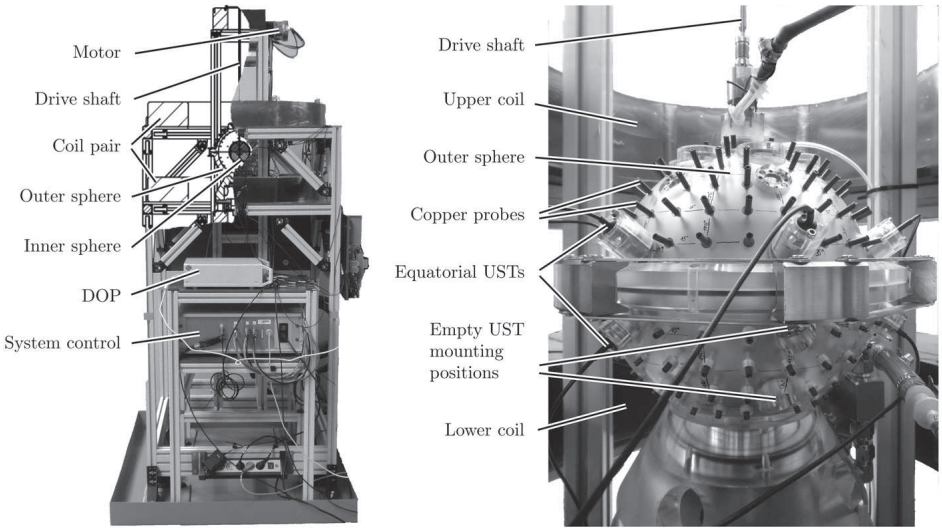

Fig. 1. The HEDGEHOG experiment: (*a*) photograph of the facility; (*b*) zoom on the spherical Couette module, showing the mountings for the ultrasound transducers (USTs) and the copper electrodes for electric potential measurements.

1. The experimental setup. Fig. 1 gives an overview of the experimental setup. The main parts, comprising the spherical vessel, the coil pair, the system controls and the diagnostics are mounted on a rack shown in the global view (Fig. 1*a*).

The central module (Fig. 1*b*) contains one of two inner spheres ($r_\mathrm{i} = 3\,\mathrm{cm}$ or $4.5\,\mathrm{cm}$) rotating in the center of an outer sphere ($r_\mathrm{o} = 9\,\mathrm{cm}$). Both spheres are made of Polymethyl Methacetate (PMMA) acrylic with 30 cylindrical holders for ultrasonic Doppler velocimetry (UDV) and 168 copper electrodes for electric potential measurement. Two 90 W motors drive the inner and outer spheres independently of each other. The outer sphere rests on a turntable connected to one motor; a 3 mm drive shaft, which widens up to 6 mm outside the shell, connects the inner sphere to the upper turntable. This paper is restricted to experiments with the outer sphere at rest and $\mathrm{Re} \leq 10^4$ ($\Omega_\mathrm{i} < 0.17\,\mathrm{Hz}$.)

The space between the two spheres is filled with GaInSn. Because of the high density of this medium ($6360\,\mathrm{kg/m^3}$), each optional inner sphere contains a lead weight to counter the buoyancy force. The axial magnetic field is provided by a pair of copper electromagnets with central radii of 30 cm and a vertical gap of 31 cm between them. This near Helmholtz configuration produces a static vertical magnetic field with less than one percent inhomogeneity in the relevant measurement volume, providing $\mathrm{Ha} \leq 160$ ($B \leq 130\,\mathrm{mT}$).

Ultrasound transducers (USTs) mounted on the outer sphere allow a wide variety of velocity field measurements from 30 different positions (five different latitudinal positions repeated at six evenly spaced longitudes, see Fig. 2). The maximum wall thickness between the UST and the fluid is 7 mm. We use USTs with 4 MHz emitting frequency and the ultrasonic Doppler velocimeter (UDV) DOP3010 (Signal Processing SA, Switzerland). In the future, a large number of installed copper pins will additionally be used as electro-static potential probes. The outer sphere and the provided measurement technique are shown in Fig. 1*b*.

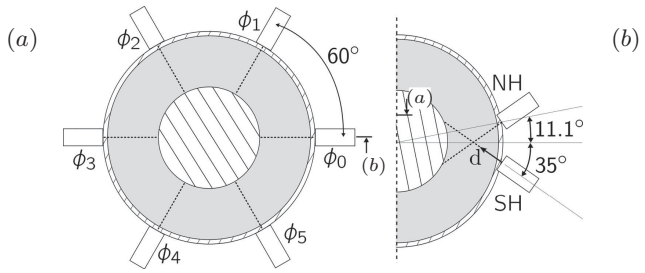

Fig. 2. UDV sensor configuration. (*a*) Polar view; (*b*) meridional view. The NH and SH sensors are positioned at angles of ±11.1° to the equator. Note, however, that their viewing angle has been chosen as ±35° to identify clearly the jet instability at low values of Ha.

2. Numerical predictions. The experiment's dynamics are described by the incompressible Navier-Stokes equation

$$\nabla \cdot \mathbf{U} = 0 \tag{1}$$

$$\frac{\partial \mathbf{U}}{\partial t} = \nabla p^* + \mathrm{Re}\,(\nabla \times \mathbf{U}) \times \mathbf{U} + \mathrm{Ha}^2\,(\nabla \times \mathbf{B}) \times \mathbf{B}, \tag{2}$$

where p^* is a reduced pressure absorbing all potential forces, and no-slip conditions at the inner and outer spheres define the drive of the flow by the rotating inner sphere. The Navier–Stokes equation couples to the magnetic induction equation in its inductionless limit

$$0 = \nabla^2 \mathbf{b} + \nabla \times (\mathbf{U} \times \mathbf{B}_0)\,. \tag{3}$$

In this limit, the generation of a magnetic field $\mathbf{b}$ from the interaction of a velocity field $\mathbf{U}$ with a background field $\mathbf{B}_0$ is exactly balanced by its diffusion. Initial simulations of the HEDGEHOG were carried out with the code described in [10]. These provided predictions of the diagnostic outputs and demonstrated a possible saturation mechanism for the instabilities [11]. Further simulations were carried out with an adapted version of the MagIC code [12], which has a long and very successful record of simulating dynamos in spherical geometry [13, 14].

Fig. 3 shows the stability boundaries and illustrates the typical instabilities for an MSC flow with the aspect ratio $\eta = 0.5$. First, Fig. 3*a* shows the boundaries for the different types of instability in the $\mathrm{Ha} - \mathrm{Re}$ plane. The lines were adapted from [6], although large parts of the diagram have been reproduced by our own simulations. The left and right full circles represent two distinct types of instability which are separated by a region of stability, represented by the middle full circle. The spatial character of the flow at these three points, as simulated by the MagIC code, is illustrated in Fig. 3*b*-*g*.

At low $\mathrm{Ha} = 5$, the instability arises in the jet connecting the equators of the inner and outer spheres, see Fig. 3*b*,*d*. It is antisymmetric with respect to the equator and characterized by an $m = 3$ azimuthal dependence. At $\mathrm{Ha} = 19.6$, the flow has completely re-stabilized. At higher $\mathrm{Ha} = 30$, another type of instability arises in the return flow, the meridional circulation through the interior of the flow that connects the equatorial jet to the pole (see Fig. 3*d*,*g*.) It is symmetric with respect to the equator and has an $m = 4$ azimuthal dependence.

3. Experimental results. Before any further evaluation, intensive post processing of the raw UDV data was necessary. The chosen pulse repetition frequency and the internal correlation algorithm cause the appearance of a broad

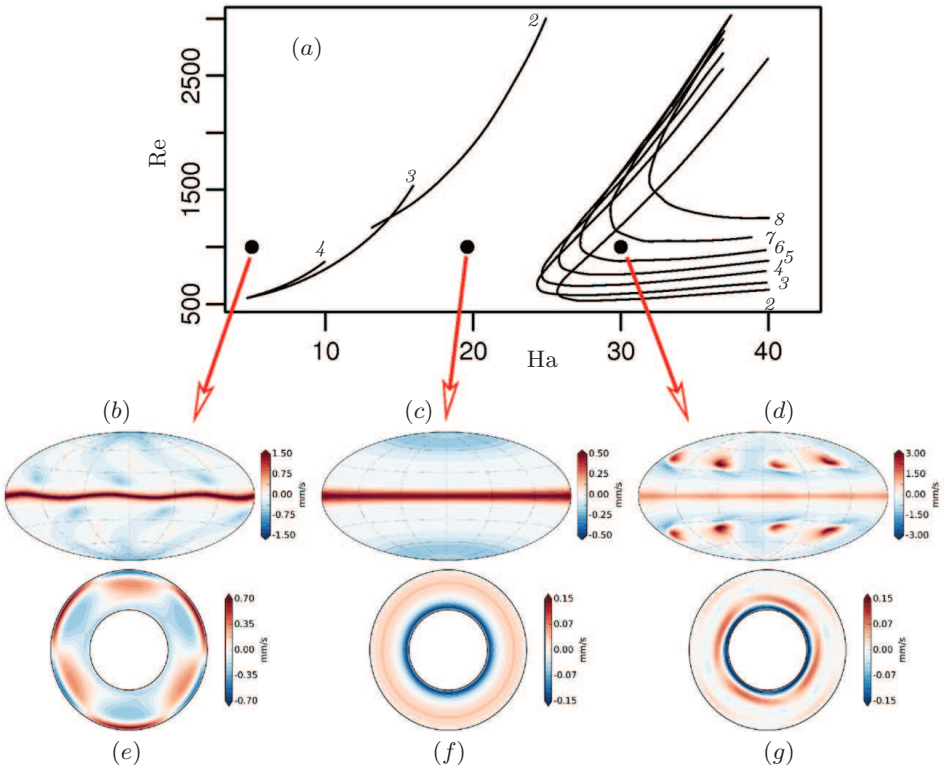

Fig. 3. Numerical simulations of the HEDGEHOG experiment. (*a*) Instability boundaries versus Ha and Re, adopted from [6] and benchmarked with a linearized Navier–Stokes equation analysis of the axisymmetric base flows [4, 10]. Left column: instability at Rm = 1000 and Ha = 5. (*b*) Meridional view of the simulated radial velocity component at $r = 0.85r_o$, showing the equatorially antisymmetric jet instability. (*e*) Polar view of the meridional velocity component at $\theta = \pi/2$ (the equatorial plane), indicating an $m = 3$ azimuthal dependence. Middle column: stable base flow at Rm = 1000 and Ha = 19.6. (*c*) Meridional view of the simulated radial velocity component at $r = 0.85r_o$. (*f*) Polar view of the meridional velocity component at $\theta = \pi/2$. Right column: instability at Rm = 1000 and Ha = 30. (*d*) Meridional view of the simulated radial velocity component at $r = 0.6r_o$, showing the equatorially symmetric character of the return flow instability. (*g*) Polar view of the meridional velocity component at $\theta = \pi/2$, indicating an $m = 4$ azimuthal dependence.

velocity range in the raw data. Moreover, the acquired data contain divers unphysical spikes, reaching values ten times higher than physically expected. Therefore, a reasonable velocity range based on $r_i\Omega$ was pre-selected, with velocities out of this range being skipped and replaced with linearly interpolated values from valid neighbouring points. The cleaned velocity is resampled onto a uniform grid and eventually smoothed by a Gaussian filter.

The data presented in the following is based on the velocity acquired from six equally spaced UDV sensors on the northern hemisphere (NH) and from one UDV sensor on the southern hemisphere (SH) (Fig. 2). Using only six sensors' data in the azimuthal direction, a maximum wave number of $m = 3$ can be resolved according to the Nyquist-Shannon criterion (this sub-sampling leads to an ambiguity in the identification of the $m = 4$ instability, as discussed below). The dominant frequency of the equatorially symmetric and antisymmetric velocity parts

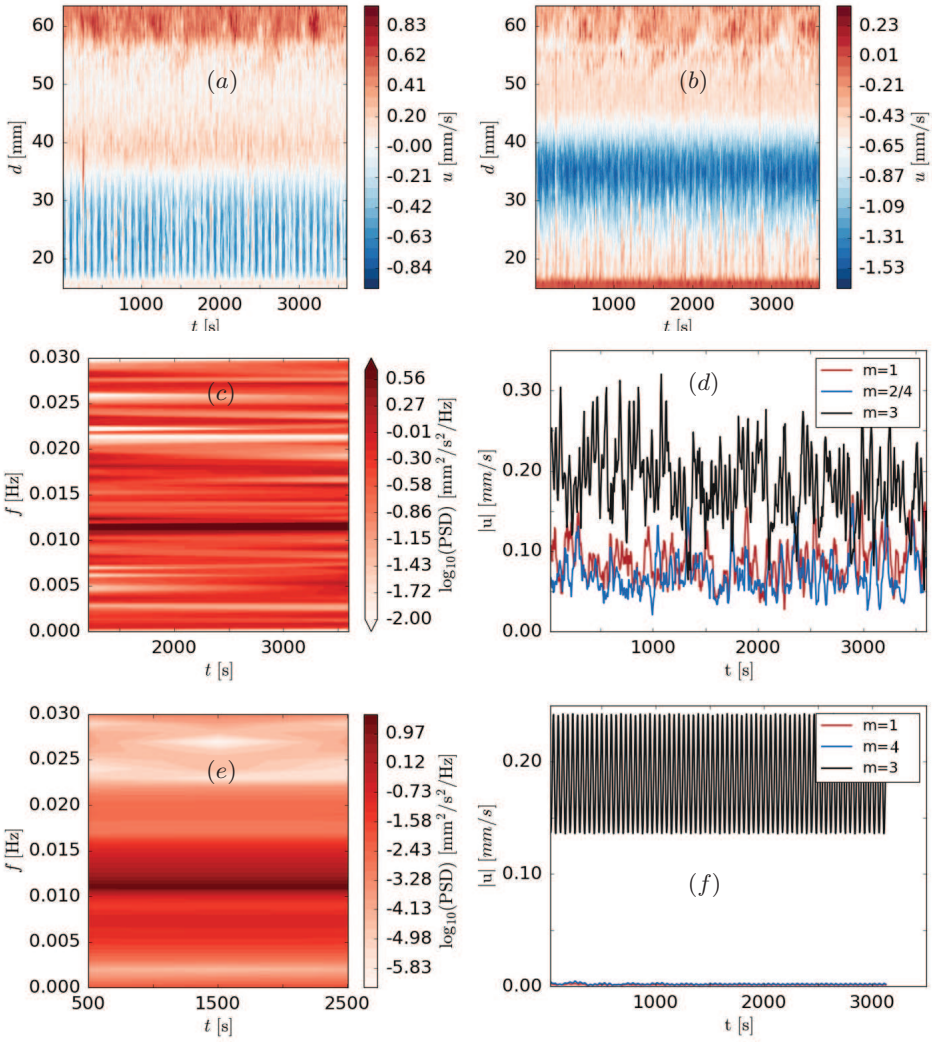

Fig. 4. Experimental and numerical data for Re = 1000 and Ha = 5. (*a*) Anti-symmetric part $(u_{\mathrm{NH}} - u_{\mathrm{SH}})/2$ of the UDV measured velocity, showing a clear oscillation in the outer part of the spherical shell, close to the equator. (*b*) Symmetric part $(u_{\mathrm{NH}} + u_{\mathrm{SH}})/2$, indicating the concentrated jet at the equator. (*c*) PSD of the anti-symmetric part taken at a UDV beam depth of $d = 25$ mm, showing a clear peak around 0.011 Hz. (*e*) The same PSD, but simulated with MagIC. (*d*) Azimuthal Fourier components of the UDV measured velocity taken at $d = 25$ mm, with the clearly dominating $m = 3$ mode. (*f*) The same for the simulated velocity with a nearly pure $m = 3$ mode.

can be inferred from spectrograms. The data from the facing NH and SH UDV pair are decomposed into equatorially symmetric and anti-symmetric components ($u_{\mathrm{s}} = (u_{\mathrm{NH}} + u_{\mathrm{SH}})/2$ and $u_{\mathrm{a}} = (u_{\mathrm{NH}} - u_{\mathrm{SH}})/2$, respectively).

In the following, we will describe three experimental runs, all done with a rotation rate of the inner sphere of 0.027 Hz, which amounts to Re = 1000. The currents in the Helmholtz coils were chosen as 12.08 A, 47.34 A, 72.47 A, corresponding to Ha = 5, 19.6, 30, respectively.

Starting at the low value Ha = 5 (see the left point and column in Fig. 3), Fig. 4 reveals the instability of the radial equatorial jet which was already known from the purely hydrodynamic case [15]. Fig. 4*a* shows the equatorially anti-

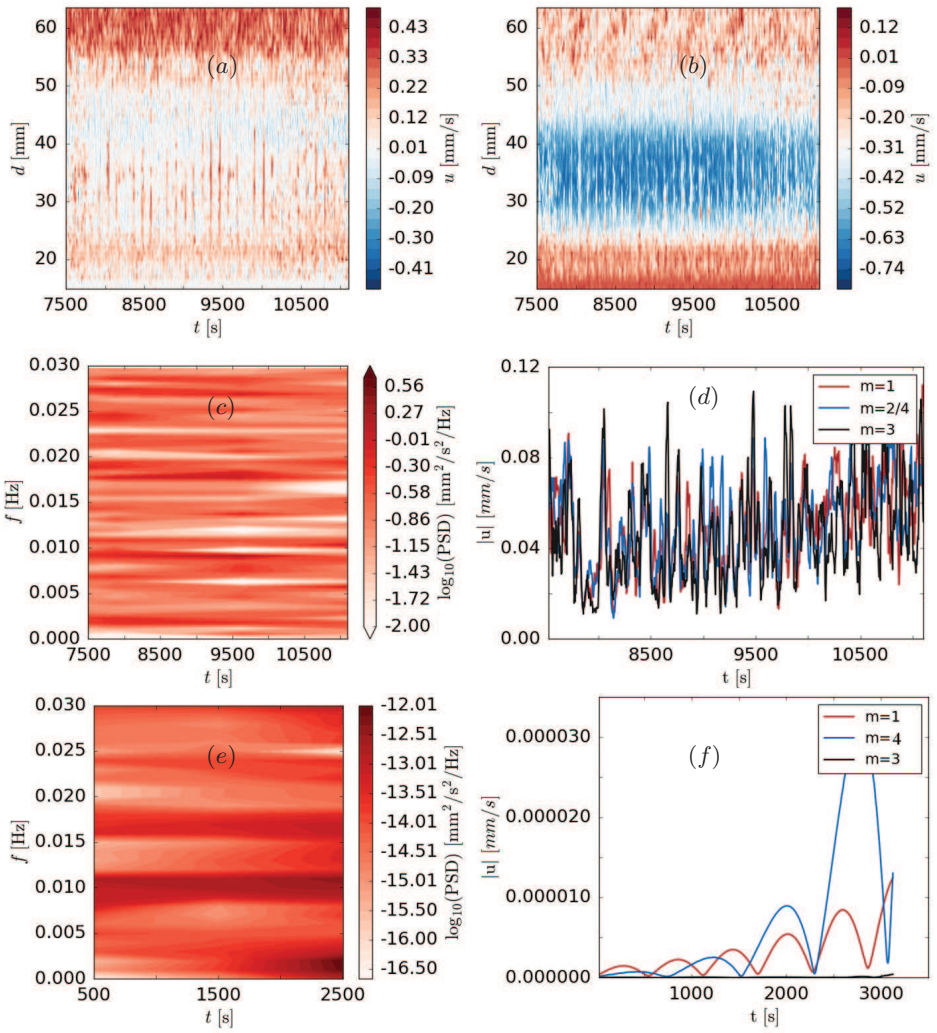

Fig. 5. Experimental and numerical data for Re = 1000 and Ha = 19.6. (*a*) Anti-symmetric part $(u_{\mathrm{NH}} - u_{\mathrm{SH}})/2$ of the UDV measured velocity. (*b*) Symmetric part $(u_{\mathrm{NH}} + u_{\mathrm{SH}})/2$. (*c*) PSD of the anti-symmetric part taken at $d = 25$ mm. (*e*) The same PSD, but simulated with MagIC. (*d*) Azimuthal Fourier components of the UDV measured velocity taken at $d = 25$ mm. (*f*) The same for the simulated velocity.

symmetric part of the UDV measured velocity, taken at the UDV beam depth $d = 25$ mm. The corresponding symmetric part is added in Fig. 4*b*. While the latter clearly shows a strong radial equatorial jet centered around $d = 35$ mm, the former shows the anti-symmetric instability slightly above and below the equator. The dominant frequency of this instability, $f \approx 0.011$ Hz, is derived from the PSD of the experimental data (Fig. 4*c*). This corresponds well to the frequency computed by the MagIC simulations (Fig. 4*e*). The azimuthal dependence of the instability can be inferred from Fig. 4*d*. At every instant in time it provides the spectral content of the first dominating azimuthal modes $m = 1$, 2, 3. Note that due to the Nyquist–Shannon theorem, we cannot distinguish between the $m = 2$ and the $m = 4$ mode, which will become relevant below. Here, the $m = 3$ mode is clearly dominant, which confirms the numerical prediction, as shown in Fig. 4*f*.

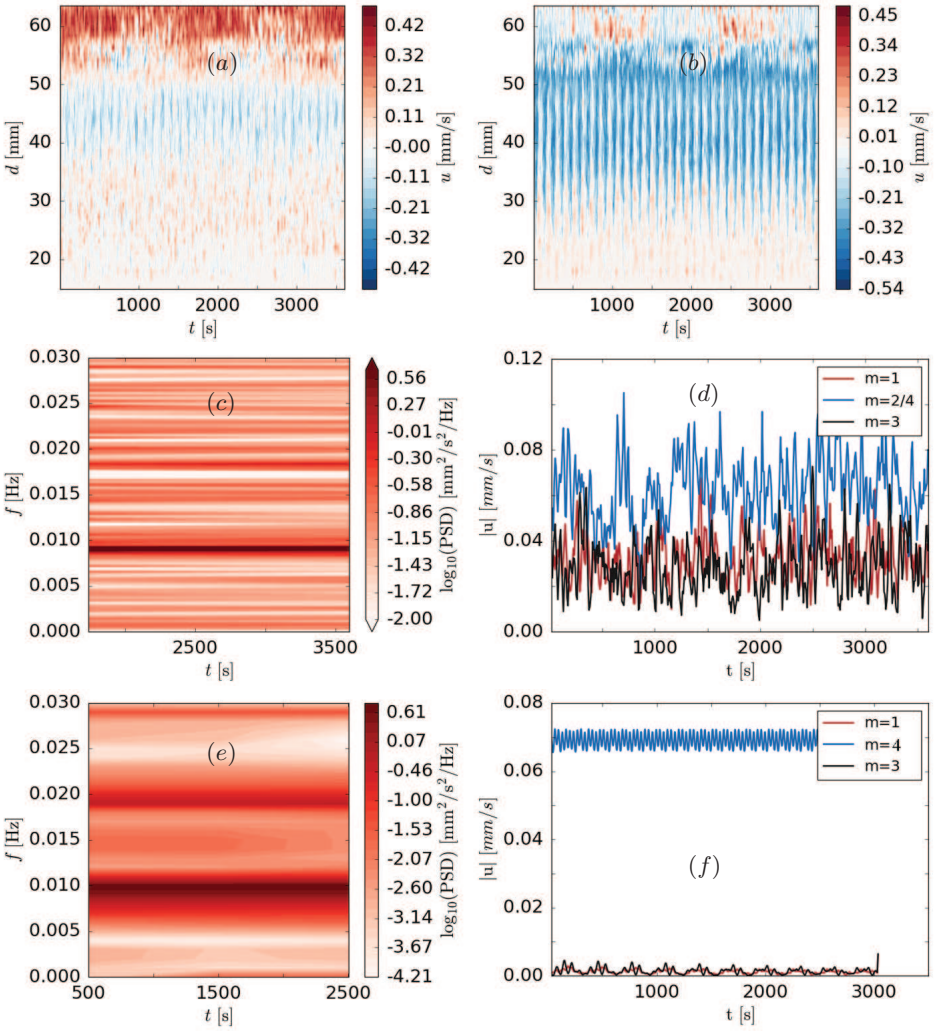

Fig. 6. Experimental and numerical data for Re = 1000 and Ha = 30. (*a*) Anti-symmetric part $(u_{\mathrm{NH}} - u_{\mathrm{SH}})/2$ of the UDV measured velocity, showing a vanishing oscillation in the outer part of the spherical shell (corresponding to the low beam depth d). (*b*) Symmetric part $(u_{\mathrm{NH}} + u_{\mathrm{SH}})/2$, indicating a clear oscillation at larger d, close to the tangential cylinder. (*c*) PSD of the symmetric part taken at $d = 37$ mm, showing a clear peak around 0.009 Hz. (*e*) The same PSD, but simulated with MagIC. (*d*) Azimuthal Fourier components of the UDV measured velocity taken at a depth of 37 mm, with dominating $m = 2/4$ mode (not distinguishable due to the Nyquist theorem). (*f*) The same for the simulated velocity, with a nearly pure $m = 4$ mode.

We switch now to the case Ha = 19.6 which lies in the isthmus of stability shown in Fig. 3 (middle column). The first observation to make is a significantly weakened (and slightly broadened) radial jet (see Fig. 5*b*, and note the changed colour scale of the velocity compared with that of Fig. 4*b*). This weakened jet is no longer unstable (Fig. 5*b*). Thus, the PSD of the data as well as the Fourier components of the different m modes are much reduced compared with those in Fig. 4.

At Ha = 30 the instability is distinctly shifted towards the inner sphere and acquires an equatorially symmetric character, which indicates the onset of return flow instability. Indeed, the anti-symmetric signal (Fig. 6*a*) is much weaker than

that in Fig. 4*a*, whereas the symmetric part (Fig. 6*b*) is significantly stronger than in Fig. 4*b*. Fig. 6*c* shows the PSD of the *symmetric* part, this time taken at a beam depth of $d = 38\,\mathrm{mm}$, with a strong peak at $f = 0.009\,\mathrm{Hz}$, which is also numerically found (Fig. 6*e*). Combined with this agreement of the frequencies, the numerically determined dominant $m = 4$ mode (Fig. 6*f*) justifies to resolve the experimental ambiguity between the $m = 2$ and the $m = 4$ mode in favour of the latter.

4. Conclusions and outlook. In this paper, we have described in detail the new MSC flow experiment HEDGEHOG. The azimuthal wave numbers and frequencies of the various instabilities for increasing Ha turned out to be in good agreement with linear and nonlinear numerical predictions. In the future, electric potential measurements might help to further reduce the remaining ambiguities with respect to the azimuthal wave number of the observed modes.

Acknowledgments. This research was supported by Deutsche Forschungsgemeinschaft (DFG) under grant STE 991/1-1. We gratefully acknowledge many discussions with Rainer Hollerbach, who also inspired us to set up the experiment. We thank Benjamin Gohl for his help in constructing the apparatus, and Johannes Wicht for sharing with us the MagIC code.

References

[1] G. Rüdiger, L.L. Kitchatinov, and R. Hollerbach. *Magnetic Processes in Astrophysics*. (Wiley-VCH, 2013).

[2] D.R. Sisan *et al.* Experimental observation and characterization of the magnetorotational instability. *Phys. Rev. Lett.*, vol. 93 (2004), Art. No. 114502.

[3] S.A. Balbus and J.F. Hawley. A powerful local shear instability in weakly magnetized disks. 1. Linear analysis. *Astrophys. J.*, vol. 376 (1991), pp. 214–222.

[4] R. Hollerbach. Non-axisymmetric instabilities in magnetic spherical Couette flow. *Proc. the Royal Society of London A: Mathematical, Physical and Engineering Sciences*, vol. 465 (2009), pp. 2003–2013.

[5] C. Gissinger, H. Ji, and J. Goodman. Instabilities in magnetized spherical Couette flow. *Phys. Rev. E*, vol. 84 (2011), Art. No. 026308.

[6] V. Travnikov, K. Eckert, and S. Odenbach. Influence of an axial magnetic field on the stability of spherical Couette flows with different gap widths. *Acta Mechanica*, vol. 219 (2011), pp. 255–268.

[7] F. Stefani *et al.* Helical magnetorotational instability in a Taylor–Couette flow with strongly reduced Ekman pumping. *Phys. Rev. E*, vol. 80 (2009), Art. No. 066303.

[8] M. Seilmayer *et al.* Experimental evidence for non-axisymmetric magnetorotational instability in an azimuthal magnetic field. *Phys. Rev. Lett.*, vol. 113 (2014), Art. No. 024505.

[9] M. Seilmayer *et al.* Experimental evidence for a transient Tayler instability in a cylindrical liquid–metal column. *Phys. Rev. Lett.*, vol. 108 (2012), Art. No. 244501.

[10] R. Hollerbach. A spectral solution of the magneto-convection equations in spherical geometry. *Int. J. Numer. Math. Fluids*, vol. 32 (2002), pp. 773–797.

[11] E. Kaplan. Saturation of non-axisymmetric instabilities of magnetized spherical Couette flow. *Phys. Rev. E* vol. 89 (2012), Art. No. 063016.

[12] https://github.com/magic-sph/magic.

[13] J. Wicht. Flow instabilities in the wide-gap spherical Couette system. *J. Fluid Mech.*, vol. 738 (2014), pp. 184–221.

[14] J. Wicht and A. Tilgner. Theory and modeling of planetary dynamos. *Space Sci. Rev.*, vol. 152 (2010), pp. 501–542.

[15] R. Hollerbach, M. Junk, and C. Egbers. Non-axisymmetric instabilities in basic state spherical Couette flow. *Fluid Dynamics Research*, vol. 38 (2006), pp. 257–273.